University of Groningen

Repeatability of arterial input functions and kinetic parameters in muscle obtained by dynamic contrast enhanced MR imaging of the head and neck

Koopman, Thomas; Martens, Roland M.; Lavini, Cristina; Yaqub, Maqsood; Castelijns, Jonas A.; Boellaard, Ronald; Marcus, J. Tim

IMPORTANT NOTE: You are advised to consult the publisher's version (publisher's PDF) if you wish to cite from it. Please check the document version below.

Document Version
Publisher's PDF, also known as Version of record

Publication date:
2020

Original Contribution

Repeatability of arterial input functions and kinetic parameters in muscle obtained by dynamic contrast enhanced MR imaging of the head and neck

Thomas Koopman[a,*], Roland M. Martens[a], Cristina Lavini[b], Maqsood Yaqub[a],
Jonas A. Castelijns[a,c], Ronald Boellaard[a,d], J. Tim Marcus[a]

[a] *Department of Radiology & Nuclear Medicine, Amsterdam UMC, Vrije Universiteit Amsterdam, de Boelelaan 1117, Amsterdam, the Netherlands*
[b] *Department of Radiology, Amsterdam UMC, University of Amsterdam, Meibergdreef 9, Amsterdam, the Netherlands*
[c] *Department of Radiology, The Netherlands Cancer Institute—Antoni van Leeuwenhoek Hospital (NKI-AVL), Plesmanlaan 121, Amsterdam, the Netherlands*
[d] *Department of Nuclear Medicine & Molecular Imaging, University Medical Center Groningen, Hanzeplein 1, Groningen, the Netherlands*

ARTICLE INFO

ABSTRACT

Background: Quantification of pharmacokinetic parameters in dynamic contrast enhanced (DCE) MRI is heavily dependent on the arterial input function (AIF). In the present patient study on advanced stage head and neck squamous cell carcinoma (HNSCC) we have acquired DCE-MR images before and during chemo radiotherapy. We determined the repeatability of image-derived AIFs and of the obtained kinetic parameters in muscle and compared the repeatability of muscle kinetic parameters obtained with image-derived AIF's versus a population-based AIF.

Materials and methods: We compared image-derived AIFs obtained from the internal carotid, external carotid and vertebral arteries. Pharmacokinetic parameters (v_e, K^{trans}, k_{ep}) in muscle—located outside the radiation area—were obtained using the Tofts model with the image-derived AIFs and a population averaged AIF. Parameter values and repeatability were compared. Repeatability was calculated with the pre- and post-treatment data with the assumption of no DCE-MRI measurable biological changes between the scans.

Results: Several parameters describing magnitude and shape of the image-derived AIFs from the different arteries in the head and neck were significantly different. Use of image-derived AIFs led to higher pharmacokinetic parameters compared to use of a population averaged AIF. Median muscle pharmacokinetic parameters values obtained with AIFs in external carotids, internal carotids, vertebral arteries and with a population averaged AIF were respectively: v_e (0.65, 0.74, 0.58, 0.32), K^{trans} (0.30, 0.21, 0.13, 0.06), k_{ep} (0.41, 0.32, 0.24, 0.18). Repeatability of pharmacokinetic parameters was highest when a population averaged AIF was used; however, this repeatability was not significantly different from image-derived AIFs.

Conclusion: Image-derived AIFs in the neck region showed significant variations in the AIFs obtained from different arteries, and did not improve repeatability of the resulting pharmacokinetic parameters compared with the use of a population averaged AIF. Therefore, use of a population averaged AIF seems to be preferable for pharmacokinetic analysis using DCE-MRI in the head and neck area.

1. Introduction

Dynamic contrast enhanced magnetic resonance imaging (DCE-MRI) can be used to estimate tissue perfusion and micro vessel permeability. The rate constants estimated using Tofts pharmacokinetic analysis of DCE-MR images (i.e. K^{trans} and k_{ep}) [1] and their ratio (v_e) reflect physiological parameters such as perfusion, permeability and cellular density, and can therefore be used to quantitatively assess these tissue properties. As reviewed by Bernstein et al., quantitative DCE-MRI biomarkers are potential predictors of prognosis and treatment response in head and neck squamous cell carcinoma (HNSCC) [2]. The validation of these biomarkers is, however, still ongoing, both in the head-and-neck region as well as in other body parts [3].

One essential requirement for the Tofts pharmacokinetic analysis is

---

the knowledge of the arterial input function (AIF). Since the obtained rate constants are heavily dependent on the AIF [4–8], an accurate and precise measurement is necessary for their absolute and reliable quantification. Alternatively, a simplified approach, such as a population averaged AIF can be used. However, (large) variabilities in cardiac output—between patients and within patients over time—are no longer taken into account with this approach. If this variability in cardiac output can be accounted for by precise measurement of the AIF, the accuracy and repeatability of the kinetic parameters should be superior over use of a population averaged AIF. Some authors have shown that a population averaged AIF can result in better repeatability [9,10], whereas others report the opposite [11,12]. It is possible that repeatability depends on the imaged body part and imaging sequence parameters, but also on the choice of the artery for AIF measurement.

As recently indicated by the quantitative imaging biomarkers alliance (QIBA) [3], the literature lacks studies on repeatability of quantitative (pharmacokinetic model derived) DCE-MRI parameters. This is especially true in the head and neck region. The repeatability of the AIF used as input for the model is also only sporadically reported [13,14]. We therefore sought to investigate both the dependence of the AIF repeatability on the choice of the artery, as well as the dependence of repeatability of the pharmacokinetic parameters on the chosen AIF.

In the present patient study on advanced stage head and neck squamous cell carcinoma (HNSCC) we have acquired DCE-MR images before and during chemo radiotherapy. Because the second MRI examination occurs during treatment, while the first occurs before, we are not able to report on the repeatability of kinetic parameters in HNSCC tumor tissue. Instead, we chose a neck muscle (left semispinalis capitis muscle) outside the radiation zone assuming that this muscle would be unaffected by the treatment and its pharmacokinetic parameters would remain unchanged between the first and the second examination.

We assessed the repeatability of the parameters describing the image-derived AIFs, measured in the internal carotids, external carotids and vertebral arteries, both on the left and right side. At the same time we assessed the repeatability of the pharmacokinetic parameters in the muscle using image-derived AIFs obtained from the internal carotids, external carotids and vertebral arteries, respectively, and compared it to that obtained using a population averaged AIF.

2. Materials and methods

The study population consisted of 29 patients with advanced stage squamous cell carcinoma who successfully underwent two MRI examinations in an ongoing prospective study. This prospective, single-center study was approved by the Medical Ethics Committee of the university and has been performed in accordance with the Declaration of Helsinki. Informed consent was acquired from all patients after full explanation of the procedures. Previously untreated patients with histologically proven HNSCC, planned for curative (chemo) radiotherapy were consecutively included from 2013 until 2018. Treatment consisted of radiotherapy (70 Gy in 35 fractions in a seven week period) with or without concomitant chemotherapy (cisplatin or cetuximab). Exclusion criteria were: nasopharyngeal tumors, age < 18 and inadequate image quality.

Baseline imaging was performed before treatment. Two weeks after start of treatment a second imaging session was performed with exactly the same MRI protocol on the same MRI scanner. The basic assumption in this study is that between both MRI examinations, there was no systematic effect of treatment on the AIF and on the contrast enhancement properties of muscle tissue outside the radiation zone. The validity of this assumption might seem questionable, because weight and muscle mass loss is a general effect of the treatment and of the disease itself [15]. However, bodyweight is a factor that is accounted for in the administration dose of the contrast agent. Moreover, given the relatively short amount of time between scans, measurable changes in healthy muscle tissue were not expected. Thus the comparison between

baseline and during treatment imaging gives the opportunity to assess repeatability of the AIF and the DCE parameters in muscle.

2.1. Imaging protocol

The DCE MRI acquisition was preceded by a variable flip angle (VFA) measurement for T_1 map estimation and followed by a B1 mapping acquisition. Sequences were acquired on a 3.0 T Ingenuity TF PET/MR-scanner (Philips Healthcare, Best, the Netherlands) equipped with a 16-channel neuro-vascular coil. Dotarem® (Guerbet, Roissy, France) was used as a gadolinium-based contrast agent. The specifications of the DCE sequence were: 3D T1-FFE (T1-weighted 3D spoiled gradient echo sequence), TR 3.1 ms, TE 1.48 ms, flip angle 12°, acquired matrix size $184 \times 169 \times 17$, acquired voxel size $1.30 \times 1.30 \times 4.40$ mm³, reconstructed matrix size $320 \times 320 \times 17$, reconstructed voxel size $0.75 \times 0.75 \times 4.40$ mm³, 75 time frames, frame duration 4.1 s. A SENSE factor of two was applied in the anterior-posterior direction. After at least four time frames, the contrast agent (0.2 ml/kg, concentration 0.5 mmol/ml) was injected at a speed of 3 ml/s using a Medrad® Spectris Solaris® power injector. A flush of 15 ml saline water was injected at 3 ml/s following the contrast bolus. The VFA measurement was acquired prior to contrast injection with settings nearly identical to the DCE protocol and five flip angles (2°, 5°, 10°, 15° and 20°). B1 mapping was performed using the method described by Yarnykh [16] (3D T1-FFE, TR_1 20 ms, TR_2 100 ms, TE 3.2 ms, flip angle 50°, acquired matrix size $176 \times 177 \times 17$, acquired voxel size $1.31 \times 1.30 \times 4.40$ mm³, reconstructed matrix size $320 \times 320 \times 17$, reconstructed voxel size $0.72 \times 0.72 \times 4.40$ mm³). The B1-map was resliced to the voxel size of the DCE image using linear interpolation and used for flip angle correction of both the DCE and VFA image. The VFA image was converted to a T_1 map using a linear least squares fit of Eq. (1) as described by Gupta [17].

The signal intensity equation for a spoiled gradient echo sequence, assuming steady state and ignoring T_2^* effects [18], is given by

$$ S = M_0 \frac{\left(1 - e^{-TR/T_1}\right) \sin\theta}{1 - e^{-TR/T_1} \cos\theta}, \tag{1} $$

where S is the signal intensity, M_0 is the thermal equilibrium magnetization and θ is the flip angle. By assuming a fast exchange regime (i.e. $T_1^{-1} = T_{10}^{-1} + r_1 C$) the contrast concentration dependent signal intensity expression (Eq. (1)) becomes

$$ S(t) = M_0 \frac{(1 - e^{-TR(T_{10}^{-1} + r_1 C(t))}) \sin\theta}{1 - e^{-TR(T_{10}^{-1} + r_1 C(t))} \cos\theta}, \tag{2} $$

where T_{10} is the pre-contrast longitudinal relaxation time, r_1 is the relaxivity of the contrast medium and C is the contrast concentration. Defining the pre-contrast signal intensity as S_0, signal enhancement can be defined as

$$ \frac{S(t) - S_0}{S_0} = \frac{(e^{-TR(T_{10}^{-1} + r_1 C(t))} - 1)\left(e^{-TR/T_{10}} \cos\theta - 1\right)}{\left(e^{-TR/T_{10}} - 1\right)(e^{-TR(T_{10}^{-1} + r_1 C(t))} \cos\theta - 1)} - 1, \tag{3} $$

such that the contrast concentration can be expressed as

$$ C(t) = \frac{1}{TR \cdot r_1} \ln\left(\frac{1 - \frac{S(t)}{S_0} \cos\theta \left(\frac{1 - e^{-TR/T_{10}}}{1 - e^{-TR/T_{10} \cos\theta}} \right)}{1 - \frac{S(t)}{S_0} \left(\frac{1 - e^{-TR/T_{10}}}{1 - e^{-TR/T_{10} \cos\theta}} \right)} \right) - \frac{1}{T_{10} \cdot r_1}. \tag{4} $$

Eq. (4) is identical to Eq. (5) from Heilmann et al. [19] and equivalent to Eq. (7) from Schabel and Parker [20].
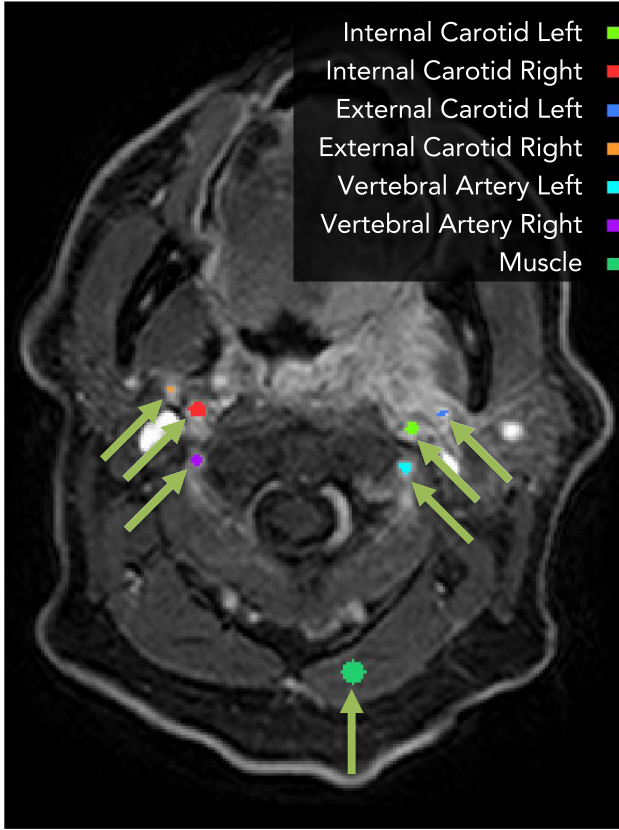
Fig. 1. Volumes of interest shown on the last dynamic frame of the DCE image. Arteries were separately delineated on the third most cranial slice, currently shown. The circular region of interest of 6 mm in diameter was placed manually in left semispinalis capitis muscle tissue on all slices except the two most cranial and two most caudal slices.

2.2. Image-derived arterial input functions

The delineated neck arteries were: vertebral arteries, internal carotids and external carotids (see Fig. 1). Each artery was manually delineated on the left and right side separately on the third most cranial slice of the image to minimize the effect of in-flow, while avoiding inaccuracies at the outer edges of the field of view. Delineation was performed using in-house developed software by a single observer in one session. The time frame of maximum enhancement in the arteries was used during delineation. The later time frames were used to identify veins, as these show a later time of contrast arrival. If the identified veins showed overlap with the delineated artery, the delineation was edited to exclude the vein from the arterial regions of interest. Images were visually inspected for movement and artefacts. Data was excluded for further analysis when movement in the arterial regions of interest was > 2 mm during the DCE image acquisition.

Signal intensities from the arteries were extracted from the dynamic contrast enhanced images by taking the average over the cross-section for each arterial region of interest. This was done for left and right regions of interest separately and for both combined, i.e. considering left and right regions as one region of interest and taking the average signal intensity of all voxels within this combined region. Enhancement of these signals over time was converted to tracer concentration using Eq. (4), defining S_0 as the average of the first four time frames and assuming a T_{10} value in blood of 1932 ms taken from literature [21]. A correction for flip angle θ was performed by using the average value of the B1-map in each arterial region of interest. A fixed hematocrit level of 0.42 was used to convert to plasma concentration as described by Parker et al. [9].
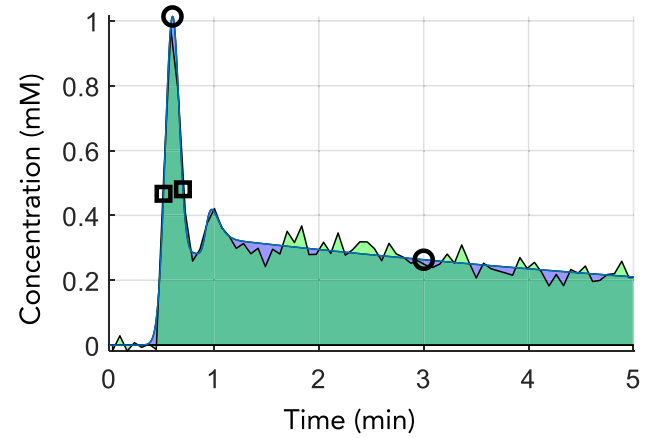
Fig. 2. Example of fitting the Parker model [9] to the image-derived AIF. The area under the fit curve is filled with blue, the area under the data is filled with green. The identified peak value and the value of the fit at 180 s are circled. The time points used for the FWHM are indicated by squares. (For interpretation of the references to color in this figure legend, the reader is referred to the web version of this article.)

Similarly to Klawer et al. [22], the resulting concentration-time curves were fitted to the model of Parker et al. [9] to extract parameters describing the magnitude and shape of the AIFs. An example of this fit is shown in Fig. 2. Several parameters were defined: maximal concentration (peak), time to peak, area under the curve (AUC), full width half maximum (FWHM), concentration at 180 s (C_{180}) and the exponential decay constant of the sigmoid modulated exponential in the Parker model, describing the tail of the concentration-time curve (washout). To ensure the FWHM only described the width of the first peak, the FWHM value was considered invalid if the value was > 30 s.

2.3. Kinetic parameters in muscle

A circular region of interest of 6 mm diameter (see Fig. 1) was placed in the left semispinalis capitis muscle on the DCE image on all slices except the two most cranial and two most caudal slices, to avoid inaccuracies at the edges of the field of view. In some patients the muscle did not lie completely in the field of view and hence less slices were included in the volume of interest. To minimize spatial mismatch, delineation of the muscle region on during treatment scans was performed while also showing the pre-treatment delineation. Signals of all voxels within the volume of interest were extracted from the DCE image and converted to concentration time curves with correction for the transmitted radiofrequency field using the B1map and using the T_{10} values from the T_1map. Mean concentration was calculated after converting to concentration for each voxel independently. Mean concentration time curves were fitted to the standard Tofts model [1] (without the vascular space) as given by

$$C_t(t) = K^{trans} \cdot e^{-k_{ep} \cdot t} \otimes C_p(t - \Delta T)$$
$$= K^{trans} \cdot \int_{\tau=0}^{t} C_p(\tau - \Delta T) \cdot e^{-k_{ep} \cdot (t-\tau)} d\tau, \tag{5}$$

where C_t is the tissue concentration time curve, C_p is the plasma concentration time curve and ΔT is the time delay between the plasma curve and arrival time in tissue. The kinetic parameters K^{trans} (rate constant from plasma to the interstitial space), k_{ep} (rate constant from the interstitial space to plasma) and v_e (fractional volume of the interstitial space and the ratio of K^{trans} and k_{ep}) were estimated. The fit was performed using a nonlinear least squares fitting procedure, constraining the kinetic parameters to positive values and using multiple starting values [23]. The model was fitted numerically using each image-derived AIF, and the population averaged AIF as described by Parker et al. [9]. All data processing was performed in Matlab, version

R2017b.

2.4. Statistical analysis

Before repeatability assessment, we checked if there were significant differences between the repeated measurements by calculating the average difference and its 95% confidence interval [24]. The repeatability of the kinetic parameters was then assessed using the within-subject coefficient of variation (wCV) [25], as calculated by Eq. (6)

$$wCV = \sqrt{\frac{1}{n} \sum_{i=1}^{n} \frac{(x_{i,1} - x_{i,2})^2/2}{((x_{i,1} + x_{i,2})/2)^2}},$$ (6)

where n is the number of patients and $x_{i,1}$ and $x_{i,2}$ are parameter values for patient i in session 1 and 2, respectively. A low value of wCV represents a high repeatability. Differences between the AIFs in descriptive parameters of the AIFs and in kinetic parameters of the muscle, and differences between wCVs were tested for significance using the nonparametric Wilcoxon matched-pairs signed ranks test. These tests were performed for left-right comparison of the three arteries, comparison between the arteries (left and right region combined of internal carotids, external carotids and vertebral arteries were compared to each other) and each artery (left and right region combined) with the population averaged AIF. The significance level was set to 0.05, after Bonferroni correction this level was 0.000397. The analyses were performed with GraphPad Prism, version 7.04.

3. Results

Data from 10 of 29 patients were excluded because movement in the arterial regions of interest was > 2 mm. Signal from the right vertebral artery of one patient could not be used because the measured enhancement was too high and conversion to concentration was not possible for the peak signal because enhancement was higher than the relationship in Eq. (3) permits. The signal of left and right vertebral artery combined was also excluded for this patient. Plots of image-derived AIFs of the internal carotids, of the tissue time-concentration curves with model fit and p-values of all tests can be found in the supplemental materials.

3.1. Image-derived arterial input functions

FWHM values were invalid for the AIF from the left internal and external carotids in one patient, from the left external carotid in another patient and from all but the left external carotid in a third patient. These AIFs showed a relatively low peak and the FWHM therefore did not describe the width of the peak. Fig. 3 shows boxplots of the parameters describing the image-derived AIFs from the pre-treatment datasets. Boxplots from the during-treatment data can be found in the supplemental material. Left-right differences were small and not significant for any of the arteries. The arterial plasma concentrations measured in this study were generally lower than the population averaged AIF measured by Parker et al., which gives an approximate plasma concentration of 10 mM at the peak and 1 mM at 180 s. The concentrations found in the current study showed median peak concentrations below 2 mM and median concentrations at 180 s below 0.5 mM for all image-derived AIFs. The parameters describing the magnitude of the AIF (i.e. peak, AUC and C180) were lower in the external carotids, higher in the vertebral arteries and intermediate in the internal carotids. These differences were significant only between the external carotids and vertebral arteries. Differences in TTP and FHWM between the different arteries were not significant. Washout was significantly different between the internal and the external carotids.

3.2. Repeatability of image-derived arterial input functions

Fig. 4 shows the repeatability of the AIF describing parameters. The parameters describing the internal carotids generally showed the best repeatability, except for the peak and TTP. No significant differences were found between arteries.

3.3. Kinetic parameters in muscle

Five out of the 38 fits to the Tofts Model (Eq. (5))—three from pre-treatment imaging, two from imaging during treatment, none of which referring to the same patient—provided unrealistic results when the population averaged AIF was used: the fitted v_e values were above 1 (range 5–160). These data were excluded from the results below. When an image-derived AIF was used these same data often—though not always—led to v_e values above 1 as well. However, because the v_e values fitted with the image-derived AIFs were in general higher than those fitted with the image-derived AIF, possibly due to underestimation of the arterial concentration as result of flow and T2 shortening, the results were only excluded if the v_e was above 3. This criterion led to exclusion of data of three patients for all image-derived AIFs and of one patient for all AIFs except those derived from the right vertebral artery and combined vertebral arteries. These four patients were also excluded when using the population averaged AIF. One additional patient was excluded for the AIF derived from the left vertebral artery.

Fig. 5 shows boxplots of the fitted pharmacokinetic parameters in the muscle before treatment. The boxplots from the during-treatment data can be found in the supplemental material. No significant differences between pre- and during-treatment data were observed. No significant differences arising from using either a left or right location of the AIF were observed in any of the parameters for any of the arteries. The values of all parameters—but most notably K^{trans}—were higher when an image-derived AIF was used, compared to those obtained using the population averaged AIF. These differences were significant for all comparisons except k_{ep} and K^{trans} between the vertebral arteries and the population averaged AIF. Comparisons between the different arteries from which the AIFs were derived showed significant differences between the vertebral arteries and the external carotids for K^{trans} and k_{ep}, but not for v_e. Values for K^{trans} and k_{ep} were the largest when using the external carotids, followed by the internal carotids and the vertebral arteries. The fitted v_e values were sometimes larger than 1 when image-derived AIFs were used, most often when using the external carotids.

3.4. Repeatability of kinetic parameters in muscle

Fig. 6 shows the repeatability of the pharmacokinetic parameters when using the various image-derived AIFs and the population averaged AIF. The wCV for each of the three parameters was lowest (i.e. highest repeatability) when a population averaged AIF was used, and highest when the AIF was derived from the vertebral arteries. However, no significant difference was observed for any of the comparisons.

4. Discussion

This study shows that image-derived AIFs obtained from different arteries in the head and neck region in the same patient differ in both magnitude and shape. Pharmacokinetic parameters in muscle, obtained using AIFs originated from different arteries, also showed significant differences. Moreover, use of a population averaged AIF led to significantly lower values of K^{trans}, k_{ep} and v_e and slightly better repeatability, although differences in repeatability between different AIF methods were not significant.
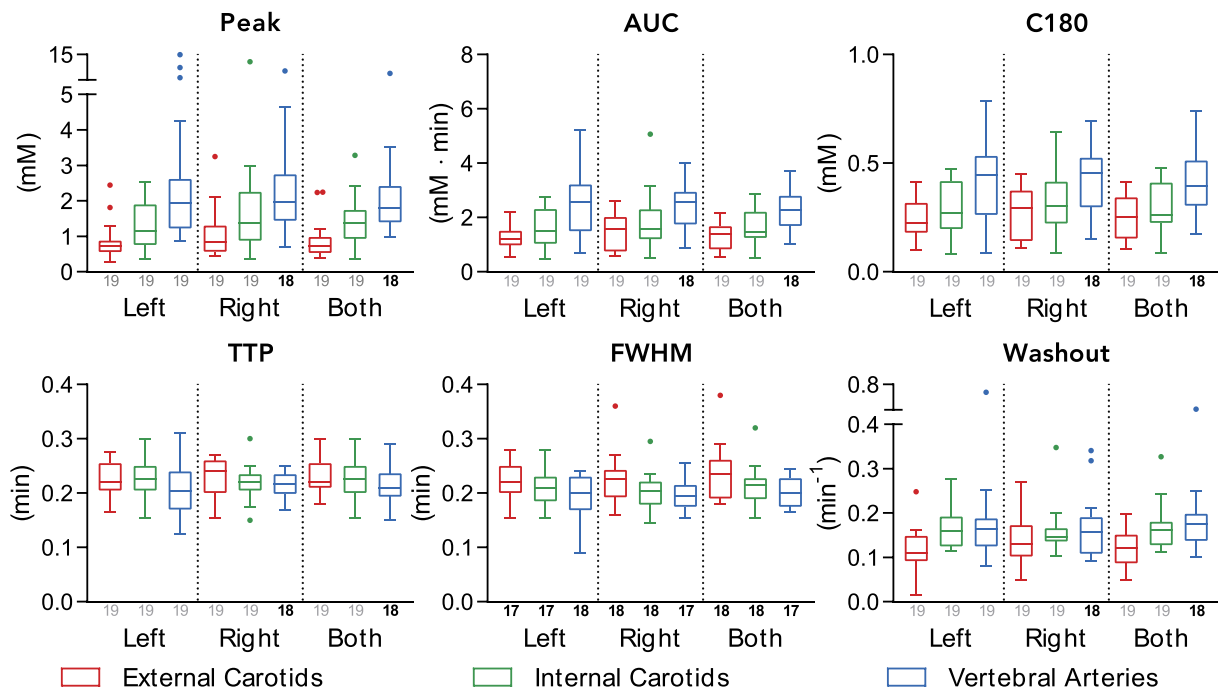
Fig. 3. Boxplots with Tukey whiskers of the parameter values describing the image-derived AIFs before treatment. Number of subjects for each boxplot is indicated by the number below it.
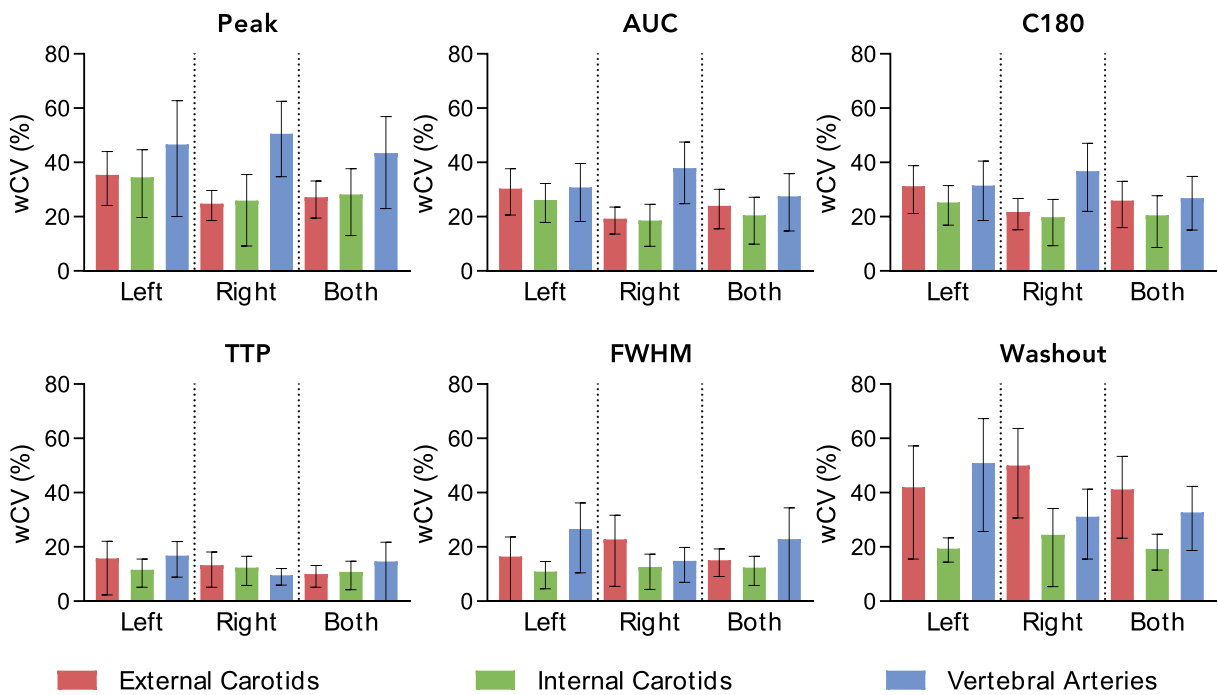

Fig. 4. Bar plots of the wCV of the descriptive parameters of the image-derived AIFs. The error bars indicate the 95% confidence interval.

4.1. Image-derived arterial input functions

The image-derived AIFs from this study seem to underestimate the arterial plasma concentration when compared to the population averaged AIF or AIFs obtained by DCE-CT [26]. Keil et al. have observed similar results in the comparison of the internal carotid, superior sagittal sinus, arteries closest to brain lesions and Parker's population averaged AIF, where arterial regions provided markedly lower concentration curves [7]. This is likely caused by blood flow artefacts and partial volume and T_2^* effects [20,27–29]. These effects are dependent

on the arterial region of interest, which may be why Parker's AIF, measured in the descending aorta, provides higher concentrations. Moreover, sensitivity for blood flow and other artefacts is dependent on the sequence settings [20]. More accurate measurements in the head and neck region might be achieved with different settings; however, this generally leads to inferior temporal and spatial resolution [20]. Additional use of phase images has been shown to lead to more repeatable AIFs which are less affected by flow [22]. In the current study, however, phase images were not available.

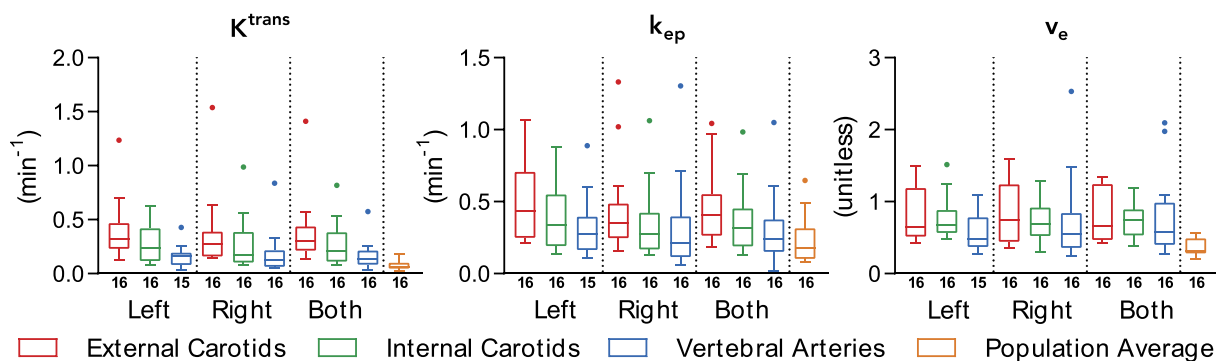While there are no significant differences in magnitude between left

Fig. 5. Boxplots with Tukey whiskers of the pharmacokinetic parameter values in the muscle before treatment. Number of subjects for each boxplot is indicated by the number below it.

and right measured AIFs, the data indicate that the magnitude and shape of an image-derived AIF are dependent on the choice of the artery. These differences are larger than what physiological differences might suggest. They might be partly explained by differences in artery diameter. Smaller arteries, such as the external carotids, are likely to be more influenced by partial volume effects, possibly resulting in lower measured concentration. Moreover, differences in flow velocities can be responsible for the differences in concentration due to the in-flow effect, possibly explaining the higher concentration in the vertebral arteries which exhibit lower flow velocity [30].

Also the repeatability of the image-derived AIF seems to be affected by the choice of artery. The internal carotids seem to give the most repeatable AIFs, especially in terms of washout. The vertebral arteries tend to have higher signal enhancement than the other arteries, suggesting that they provide more accurate concentration values. However, this may also be the reason for the poorer repeatability of the AIFs from the vertebral arteries: because the relationship between signal enhancement and concentration in Eq. (3) is nonlinear and flattens at higher concentrations of contrast agent, the value of the estimated concentration at low T1 (high concentrations) is more sensitive to noise. This results in increased concentration variability. Use of a low dose pre-bolus scan can (partially) resolve this saturation effect and may lead to more repeatable AIFs [31–35]. One other study measured AIFs in the carotids at multiple time points (to generate a population averaged AIF); however, repeatability of the individual measurements was not investigated [36].

4.2. Kinetic parameters in muscle

The differences in the parameters describing the image-derived AIFs seemed to propagate into the resulting pharmacokinetic parameters. Use of an image-derived AIF leads to significantly higher parameter values compared with using a population-based AIF, especially for

K^{trans}. This is caused by the lower amplitude of the image-derived AIFs, as discussed above.

Although the resulting pharmacokinetic values are different, in terms of repeatability no significant differences between them were found when using the different AIFs. The repeatability of k_{ep} and v_e was comparable when using either a population averaged AIF or an AIF derived from the internal carotids. This result differs from the study of Rijpkema et al. [11], who found that repeatability of k_{ep} was better if individual AIFs were used. In their dataset, 6 patients are included with a tumor in the head and neck region; however, a different sequence is used (the flip angle is particularly different) and this may explain the disparity with our study. Peled et al. [5] also found that k_{ep} repeatability improved by using individual AIFs, although their study covers the prostate. In accordance with some literature [9,10], but contradicting other [12], the repeatability of K^{trans} seems to improve when a population averaged AIF is used. Ideally, use of an image-derived AIF corrects for variability in cardiac output within the patients over time, thus leading to a better repeatability of the pharmacokinetic parameters. Apparently, however, the variability introduced by the AIF measurement counteracts this effect. Variability could be caused by partial volume effects, B1 errors and flow enhancement artefacts. Because this is different for other acquisition settings, the generalizability of our results is limited.

When the population averaged AIF was used, the tissue curves in five subjects were fitted with v_e above 1, indicating that the data do not adhere to the theoretical model, either because the population averaged AIF cannot lead to the tissue time-concentration curve, or the tissue time-concentration curve is incorrect. The latter might be explained by inaccurate T_1 estimation or errors in B1 that are not accounted for by the B1 correction. This would explain why the model also produced outliers when the image-derived AIFs were used in four of the five cases. In one case the image-derived AIFs showed a dispersed shape and fitting led to reasonable pharmacokinetic parameter values and a better
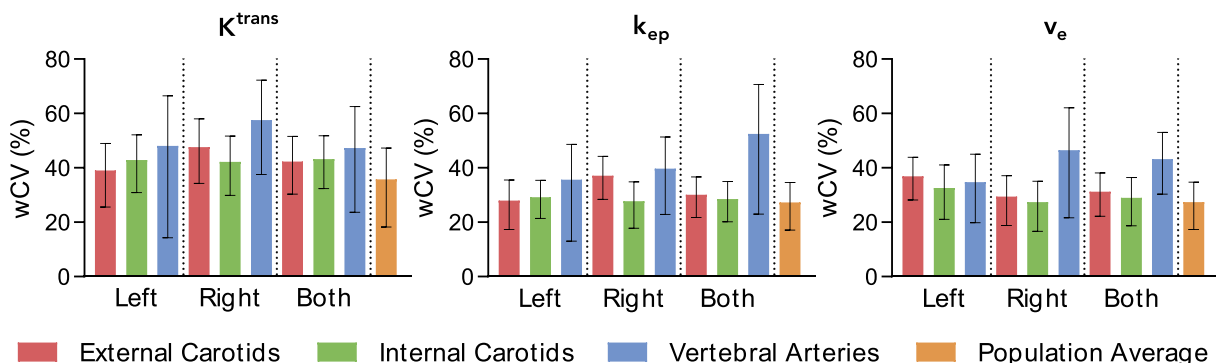

Fig. 6. Bar plots of the wCV of the muscle pharmacokinetic parameters. The error bars indicate the 95% confidence interval.

fit, indicating that use of a population averaged AIF was inappropriate in this case.

4.3. Limitations

More than one third of the data could not be evaluated. Deriving the AIF from the image is problematic when the patient moves or swallows during acquisition. Motion correction for these, often small and quick, movements is not straightforward and was not performed in this study. Use of a population averaged AIF largely overcomes this problem, although movement can also affect signals from the tissue.

Repeatability estimates within tumor and lymph nodes are necessary for biomarker validation of DCE-MRI pharmacokinetic parameters in the head and neck cancer, such as HNSCC. However, due to the setup of this study such estimates could not be investigated, because between baseline and follow-up the patients underwent chemo radiotherapy. Moreover, the repeatability estimates reported for muscle cannot be extrapolated to, for example, tumor tissue; the different tissue characteristics in tumor (or tissues in which they arise) lead to different pharmacokinetic parameter values and their repeatability is likely different [37]. The semispinalis capitis muscle was chosen as it is located outside the radiated area. However, the combination of (chemo) radiotherapy and the ongoing disease might have some systemic effects, even within this short period of time between scans. As reported, no significant differences were found between pre- and during-treatment kinetic parameters in muscle; however, if the effects of disease and therapy caused an increased variability, the wCV's reported here may be overestimated. Nonetheless, we believe that the repeatability of the pharmacokinetic parameters in the muscle region can still be a useful tool for comparison of the use of different AIFs as input of the model.

5. Conclusion

Significant variations were found in the AIFs obtained from different arteries in the head and neck region. Image-derived AIFs measured in the internal carotids show a trend to better repeatability for both the AIF itself and for the pharmacokinetic parameters estimated in muscle tissue. However, the image-derived AIF does not improve repeatability of the pharmacokinetic parameters compared to a population averaged AIF. Moreover, patient movement during acquisition, which can be common in the head and neck region, is likely to disturb AIF measurement. For these reasons, the use of a population averaged AIF in this patient population seems to be preferable for pharmacokinetic analysis of DCE-MRI when absolute PK parameter values are not of major concern.

Funding

CRediT authorship contribution statement

Thomas Koopman: Software, Formal analysis, Investigation, Writing - original draft.**Roland M. Martens:**Investigation, Writing - review & editing.**Cristina Lavini:**Methodology, Writing - review & editing.**Maqsood Yaqub:**Writing - review & editing.**Jonas A. Castelijns:**Writing - review & editing, Funding acquisition.**Ronald Boellaard:**Conceptualization, Writing - review & editing, Funding acquisition.**J. Tim Marcus:**Conceptualization, Investigation, Writing - review & editing.

Declaration of competing interest

The authors declare that they have no conflict of interest.

References

[1] Tofts PS, Brix G, Buckley DL, Evelhoch JL, Henderson E, Knopp MV, et al. Estimating kinetic parameters from dynamic contrast-enhanced t1-weighted MRI of a diffusable tracer: Standardized quantities and symbols. J Magn Reson Imaging 1999;10:223–32. https://doi.org/10.1002/(SICI)1522-2586(199909)10:3<223::AID-JMRI2>3.0.CO;2-S.

[2] Bernstein JM, Homer JJ, West CM. Dynamic contrast-enhanced magnetic resonance imaging biomarkers in head and neck cancer: potential to guide treatment? A systematic review. Oral Oncol 2014;50:963–70. https://doi.org/10.1016/j.oraloncology.2014.07.011.

[3] Shukla-Dave A, Obuchowski NA, Chenevert TL, Jambawalikar S, Schwartz LH, Malyarenko D, et al. Quantitative imaging biomarkers alliance (QIBA) recommendations for improved precision of DWI and DCE-MRI derived biomarkers in multicenter oncology trials. J Magn Reson Imaging 2019;49:e101–21. https://doi.org/10.1002/jmri.26518.

[4] Lavini C. Simulating the effect of input errors on the accuracy of Tofts' pharmacokinetic model parameters. Magn Reson Imaging 2015;33:222–35. https://doi.org/10.1016/j.mri.2014.10.004.

[5] Peled S, Vangel M, Kikinis R, Tempany CM, Fennessy FM, Fedorov A. Selection of fitting model and arterial input function for repeatability in dynamic contrast-enhanced prostate MRI. Acad Radiol 2019;26:e241–51. https://doi.org/10.1016/j.acra.2018.10.018.

[6] Huang W, Chen Y, Fedorov A, Li X, Jajamovich GH, Malyarenko DI, et al. The impact of arterial input function determination variations on prostate dynamic contrast-enhanced magnetic resonance imaging pharmacokinetic modeling: a multicenter data analysis challenge. Tomogr Ann Arbor Mich 2016;2:56–66. https://doi.org/10.18383/j.tom.2015.00184.

[7] Keil VC, Mädler B, Gieseke J, Fimmers R, Hattingen E, Schild HH, et al. Effects of arterial input function selection on kinetic parameters in brain dynamic contrast-enhanced MRI. Magn Reson Imaging 2017;40:83–90. https://doi.org/10.1016/j.mri.2017.04.006.

[8] Azahaf M, Haberley M, Betrouni N, Ernst O, Behal H, Duhamel A, et al. Impact of arterial input function selection on the accuracy of dynamic contrast-enhanced MRI quantitative analysis for the diagnosis of clinically significant prostate cancer: impact of AIF on K^trans in PCa. J Magn Reson Imaging 2016;43:737–49. https://doi.org/10.1002/jmri.25034.

[9] Parker GJM, Roberts C, Macdonald A, Buonaccorsi GA, Cheung S, Buckley DL, et al. Experimentally-derived functional form for a population-averaged high-temporal-resolution arterial input function for dynamic contrast-enhanced MRI. Magn Reson Med 2006;56:993–1000. https://doi.org/10.1002/mrm.21066.

[10] Rata M, Collins DJ, Darcy J, Messiou C, Tunariu N, Desouza N, et al. Assessment of repeatability and treatment response in early phase clinical trials using DCE-MRI: comparison of parametric analysis using MR- and CT-derived arterial input functions. Eur Radiol 2016;26:1991–8. https://doi.org/10.1007/s00330-015-4012-9.

[11] Rijpkema M, Kaanders JHAM, Joosten FBM, van der Kogel AJ, Heerschap A. Method for quantitative mapping of dynamic MRI contrast agent uptake in human tumors. J Magn Reson Imaging 2001;14:457–63. https://doi.org/10.1002/jmri.1207.

[12] Ashton E, Raunig D, Ng C, Kelcz F, McShane T, Evelhoch J. Scan-rescan variability in perfusion assessment of tumors in MRI using both model and data-derived arterial input functions. J Magn Reson Imaging 2008;28:791–6. https://doi.org/10.1002/jmri.21472.

[13] Lavini C, Verhoeff JJC. Reproducibility of the gadolinium concentration measurements and of the fitting parameters of the vascular input function in the superior sagittal sinus in a patient population. Magn Reson Imaging 2010;28:1420–30. https://doi.org/10.1016/j.mri.2010.06.017.

[14] Mendichovszky IA, Cutajar M, Gordon I. Reproducibility of the aortic input function (AIF) derived from dynamic contrast-enhanced magnetic resonance imaging (DCE-MRI) of the kidneys in a volunteer study. Eur J Radiol 2009;71:576–81. https://doi.org/10.1016/j.ejrad.2008.09.025.

[15] Willemsen ACH, Hoeben A, Lalisang RI, Van Helvoort A, Wesseling FWR, Hoebers F, et al. Disease-induced and treatment-induced alterations in body composition in locally advanced head and neck squamous cell carcinoma. J Cachexia Sarcopenia Muscle 2019. https://doi.org/10.1002/jcsm.12487.

[16] Yarnykh VL. Actual flip-angle imaging in the pulsed steady state: a method for rapid three-dimensional mapping of the transmitted radiofrequency field. Magn Reson Med 2007;57:192–200. https://doi.org/10.1002/mrm.21120.

[17] Gupta RK. A new look at the method of variable nutation angle for the measurement of spin-lattice relaxation times using Fourier transform NMR. J Magn Reson 1969 1977;25:231–5. https://doi.org/10.1016/0022-2364(77)90138-X.

[18] Wehrli FW. Fast-Scan Magnetic Resonance - Principles and Applications. 1st ed New York: Raven Press; 1991. p. 12.

[19] Heilmann M, Kiessling F, Enderlin M, Schad LR. Determination of pharmacokinetic parameters in DCE MRI: consequence of nonlinearity between contrast agent concentration and signal intensity. Invest Radiol 2006;41:536–43. https://doi.org/10.1097/01.rli.0000209607.99200.53.

[20] Schabel MC, Parker DL. Uncertainty and bias in contrast concentration measurements using spoiled gradient echo pulse sequences. Phys Med Biol 2008;53:2345–73. https://doi.org/10.1088/0031-9155/53/9/010.

[21] Stanisz GJ, Odrobina EE, Pun J, Escaravage M, Graham SJ, Bronskill MJ, et al. T1, T2 relaxation and magnetization transfer in tissue at 3T. Magn Reson Med 2005;54:507–12. https://doi.org/10.1002/mrm.20605.

[22] Klawer EME, van Houdt PJ, Simonis FFJ, van den Berg CAT, Pos FJ, Heijmink SWTPJ, et al. Improved repeatability of dynamic contrast-enhanced MRI using the

complex MRI signal to derive arterial input functions: a test-retest study in prostate cancer patients. Magn Reson Med 2019;81:3358–69. https://doi.org/10.1002/mrm.27646.

[23] Yaqub M, Boellaard R, Kropholler MA, Lammertsma AA. Optimization algorithms and weighting factors for analysis of dynamic PET studies. Phys Med Biol 2006;51:4217–32. https://doi.org/10.1088/0031-9155/51/17/007.

[24] Bland JM, Altman DG. Measuring agreement in method comparison studies. Stat Methods Med Res 1999;8:135–60. https://doi.org/10.1177/096228029900800204.

[25] Bland M. How should I calculate a within-subject coefficient of variation? https://www-users.york.ac.uk/~mb55/meas/cv.htm; 2006, Accessed date: 12 August 2019.

[26] Simonis FFJ, Sbrizzi A, Beld E, Lagendijk JJW, van den Berg CAT. Improving the arterial input function in dynamic contrast enhanced MRI by fitting the signal in the complex plane: improving AIF in DCE-MRI by fitting the complex signal. Magn Reson Med 2016;76:1236–45https://doi.org/10.1002/mrm.26023.

[27] Garpebring A, Wirestam R, Östlund N, Karlsson M. Effects of inflow and radio-frequency spoiling on the arterial input function in dynamic contrast-enhanced MRI: a combined phantom and simulation study. Magn Reson Med 2011;65:1670–9. https://doi.org/10.1002/mrm.22760.

[28] Roberts C, Little R, Watson Y, Zhao S, Buckley DL, Parker GJM. The effect of blood inflow and B_1-field inhomogeneity on measurement of the arterial input function in axial 3D spoiled gradient echo dynamic contrast-enhanced MRI: AIF errors in DCE-MRI. Magn Reson Med 2011;65:108–19. https://doi.org/10.1002/mrm.22593.

[29] van Schie JJN, Lavini C, van Vliet LJ, Vos FM. Estimating the arterial input function from dynamic contrast-enhanced MRI data with compensation for flow enhancement (I): theory, method, and phantom experiments: flow AIF 1. J Magn Reson Imaging 2018;47:1190–6. https://doi.org/10.1002/jmri.25906.

[30] Yazıcı B, Erdoğmuş B, Tugay A. Cerebral blood flow measurements of the extracranial carotid and vertebral arteries with Doppler ultrasonography in healthy adults. Diagn Interv Radiol 2005;11:195–8.

[31] Makkat S, Luypaert R, Sourbron S, Stadnik T, De Mey J. Assessment of tumor blood flow in breast tumors with T1-dynamic contrast-enhanced MR Imaging: impact of dose reduction and the use of a prebolus technique on diagnostic efficacy. J Magn Reson Imaging 2010;31:556–61. https://doi.org/10.1002/jmri.22077.

[32] Risse F, Semmler W, Kauczor H-U, Fink C. Dual-bolus approach to quantitative measurement of pulmonary perfusion by contrast-enhanced MRI. J Magn Reson Imaging 2006;24:1284–90https://doi.org/10.1002/jmri.20747.

[33] Christian TF, Aletras AH, Arai AE. Estimation of absolute myocardial blood flow during first-pass MR perfusion imaging using a dual-bolus injection technique: comparison to single-bolus injection method. J Magn Reson Imaging 2008;27:1271–7. https://doi.org/10.1002/jmri.21383.

[34] Köstler H, Ritter C, Lipp M, Beer M, Hahn D, Sandstede J. Prebolus quantitative MR heart perfusion imaging: prebolus quantitative MR heart perfusion. Magn Reson Med 2004;52:296–9. https://doi.org/10.1002/mrm.20160.

[35] Oechsner M, Mühlhäusler M, Ritter CO, Weininger M, Beissert M, Jakob PM, et al. Quantitative contrast-enhanced perfusion measurements of the human lung using the prebolus approach. J Magn Reson Imaging 2009;30:104–11. https://doi.org/10.1002/jmri.21793.

[36] Onxley JD, Yoo DS, Muradyan N, MacFall JR, Brizel DM, Craciunescu OI. Comprehensive population-averaged arterial input function for dynamic con-trast–enhanced vMagnetic resonance imaging of head and neck cancer. Int J Radiat Oncol 2014;89:658–65. https://doi.org/10.1016/j.ijrobp.2014.03.006.

[37] Galbraith SM, Lodge MA, Taylor NJ, Rustin GJS, Bentzen S, Stirling JJ, et al. Reproducibility of dynamic contrast-enhanced MRI in human muscle and tumours: comparison of quantitative and semi-quantitative analysis. NMR Biomed 2002;15:132–42. https://doi.org/10.1002/nbm.731.